Tribol Lett (2010) 37:261–272
DOI 10.1007/s11249-009-9518-3

ORIGINAL PAPER

Experimental Study and Numerical Simulation of the Large-Scale Testing of Polymeric Composite Journal Bearings: Two-Dimensional Modeling and Validation

A. Rezaei · W. Ost · W. Van Paepegem · J. Degrieck · P. De Baets

Received: 7 July 2009 / Accepted: 10 September 2009 / Published online: 23 September 2009

Abstract The self-lubricating properties of some polymeric materials make them very valuable in bearing applications, where the lubrication is difficult or impossible. Composite bearings combine the self-lubricating properties of polymeric materials with better mechanical and thermal properties of the fibers. At present, there are few studies about these bearings and their design is mainly based on manufacturers' experiences. This study includes an experimental and numerical study of the large-scale testing of fiber-reinforced polymeric composite bearings. In the first part of this article, a new tribological test setup for large composite bearings is demonstrated. Besides, a two-dimensional finite-element model is developed in order to study the stress distribution in the composite bearing and kinematics of the test setup. A mixed Lagrangian–Eulerian formulation is used to simulate the rotation of the shaft and the contact between the composite bearing and the shaft. Simulation results correspond closely to the experimental data, and provide careful investigation of the stress distribution in the bearing. In the second part of this article, three-dimensional quasi-static and two-dimensional dynamic models are studied.

Keywords Self-lubricating composites · Finite-element analysis · Friction test methods

A. Rezaei (✉) · W. Van Paepegem · J. Degrieck
Department of Materials Science and Engineering, Ghent University, Sint-Pietersnieuwstraat 41, 9000 Ghent, Belgium
e-mail: ali.rezaei@ugent.be

W. Ost · P. De Baets
Department of Mechanical Construction and Production, Ghent University, Sint-Pietersnieuwstraat 41, 9000 Ghent, Belgium

1 Introduction

Bearings accommodate the relative motion of mechanical components, either in rotational or translational motion. They are produced in different material types, shapes, and sizes. Currently besides the traditional metallic and polymer-based bearings, composite bearings are getting more and more popular. Despite the fact that the metallic bearings can carry very high loads, they have a high coefficient of friction (COF) and need to be lubricated frequently. Not only lubricating and careful maintenance of metallic bearings is expensive, but also in some cases it is impossible, for example in food industry. Contrary to the metallic bearings, polymer-based bearings have a low COF and do not need to be lubricated, but they are not able to carry heavy loading conditions.

To overcome the aforementioned problems, in recent years manufacturers have developed composite bearings, which principally are reinforced polymeric bearings. Composite bearings combine the self-lubricating properties of the polymeric materials with better mechanical properties of fibers. They are used in many industrial applications, and are able to operate under conditions in which conventional bearings cannot. These bearings are used in marine applications where it is difficult to install conventional lubricated bearings due to the presence of seawater. In food processing equipments, the absence of external lubrication makes composite bearings favorable. Their good corrosion resistance makes them appropriate for applications under water or in wet–dry situations. In addition, composite bearings can be applied in situations where traditional materials, when misaligned, are subjected to an inadmissible high edge pressure [1]. Other typical applications for composite bearings include steering linkages, hydraulic cylinder hinges, king-pins, construction and

agriculture equipments, valve bodies, off-road vehicles, windmills, material handling equipments, scissor lifts, textile equipments, tire presses, and packing machinery [2]. Among several types of plastics for bearings, phenolic polymers are commonly used because they operate satisfactorily in combination with steel shafts.

Recently, researchers tried to study the tribological properties of fiber-reinforced composite bearings from different aspects. Kawaakme and Bressan [3] have experimentally investigated the wear resistance of self-lubricating polymeric composites for application in seals of electric motors. Liu and Schaefer [4] have studied the sliding friction of three commercial thermoplastic polymer composites. Elsayed and Elsherbiny [5] have experimentally studied two types of polymeric composite bearings with polyester matrix and unidirectional linen and jute reinforcements. Friedrich et al. [6] have evaluated the mechanical properties of compacted wear debris layers, formed between composite and steel in sliding contact. The other study of Friedrich in collaboration with Goda [7, 8] describes numerical and experimental analysis of the fiber–matrix debonding in unidirectional polymer composites. Kim and Lee have worked on the designing parameters of a hybrid carbon/phenolic-laminated composite journal bearings [9]. They have also investigated the stress distribution in the asbestos–phenolic composite journal bearings [10].

At present, there are few numerical studies about composite bearings, and the degradation and wear mechanisms of these bearings are hardly understood. The bearing geometry, fiber parameters, and type of polymer are mainly determined by manufacturer's experience on trial-and-error base.

In this article, the mechanical behavior of a phenolic composite bearing with polyester fibers and PTFE filler is studied, both experimentally and numerically. To this purpose, a new test apparatus is designed and manufactured. The test rig has been designed to determine the tribological behavior of large-scale journal bearings subjected to rotational reciprocating movement.

In conventional tribotesting, small-scale tests are mainly used because of their cost effectiveness, time efficiency, and the easiness of handling of small samples. However, because clearances and pressure distribution cannot be always scaled properly, conditions can strongly differ from the real application scale, and extrapolating toward the real working conditions occasionally results in significant errors. From this point of view, experimental setups in which full-scale bearings can be tested statically and dynamically are very important. A test rig should be able to measure the friction torque accurately between journal and bearing. Usually, indirect methods are used in test rigs for journal bearings, and only few can measure friction torques by direct methods [11]. In indirect methods, the measured torque includes the friction of both the test bearing and the shaft-supporting bearings. These two elements cannot be separated in an easy way. The new test setup uses a direct method, where the friction torque of only the test bearing is measured without any interference of the shaft-supporting bearings.

Although the experimental method provides the required information to study the magnitude of the forces on the bearing, it does not give detailed information about the stresses in the contact area between the bearing and the shaft. Moreover, the experimental tests are expensive and time consuming. Hence, in order to study the distribution of the shear stresses, the normal stresses, and the effects of the allocated tolerances in the setup, numerical simulations are employed. In the first part of this article, the kinematics of the test rig is simulated with a simplified two-dimensional plane strain model by FEM method. The simulation is done as a quasi-static process with mixed Lagrangian–Eulerian approach. In the second part, the three-dimensional and dynamic modeling of the setup are studied.

2 Test Rig

The experimental studies are done with a new apparatus which is designed to determine the tribological behavior of large-scale journal bearings subjected to a reciprocating angular movement. Figure 1 shows the test rig and its cross-sectional view. This apparatus has been considered to test composite bearings with an inner diameter of 300 mm. The test is started by applying the vertical force on the bushing component by a hydraulic actuator, and then the drive piston starts to reciprocate and makes the rotational oscillation in the shaft. Figure 2 shows a schematic of the test rig's application.

The loading actuator is a hydraulic piston with a maximum load of 1500 kN. Its displacement is measured by a magnetostrictive built-in sensor, and load is measured by the load-cell, mounted between actuator and transmission trolley.

The most noticeable specifications of the apparatus are as below.

- The loading conditions, rotation speed, and rotation angle can be changed by the user at any time during the test.
- The friction torque is determined by measuring the force acting on a lever arm connected to the bushing.
- The tests are driven by a closed-loop servo-hydraulic system.
- All measuring signals are registered continuously and digitally by means of a data acquisition card.

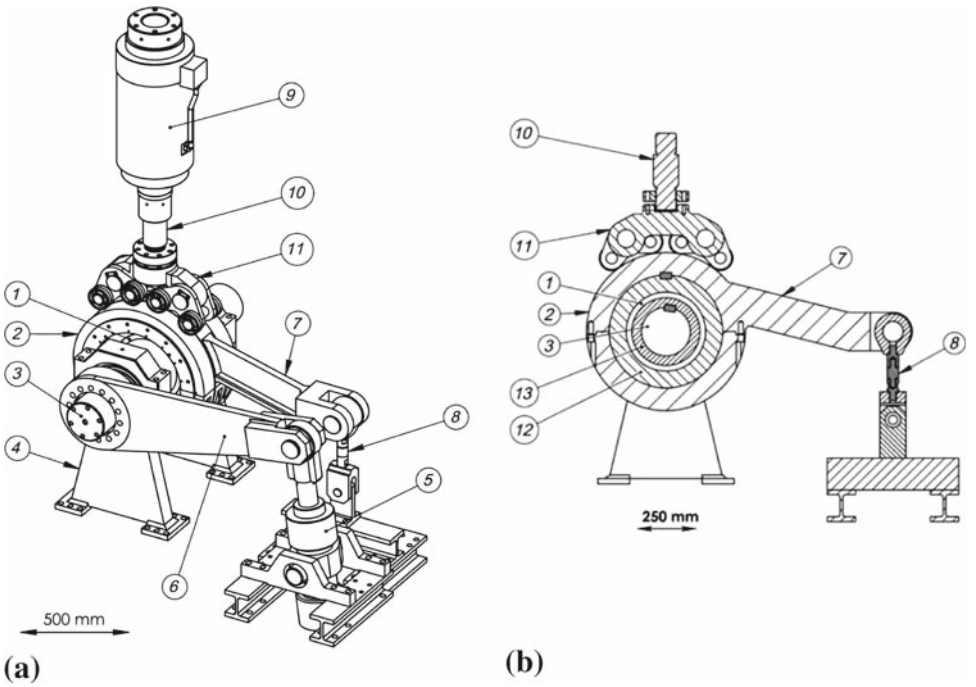

Fig. 1 **a** Components of the test setup. **b** Cross-sectional view

1	Composite bearing	8	Load-cell(friction torque)
2	Bushing	9	Hydraulic actuator
3	Shaft	10	Load-cell (vertical load)
4	Shaft support	11	Load transmission trolley
5	Drive piston	12	Backing
6	Drive lever arm	13	Shaft bushing
7	Bushing lever arm		

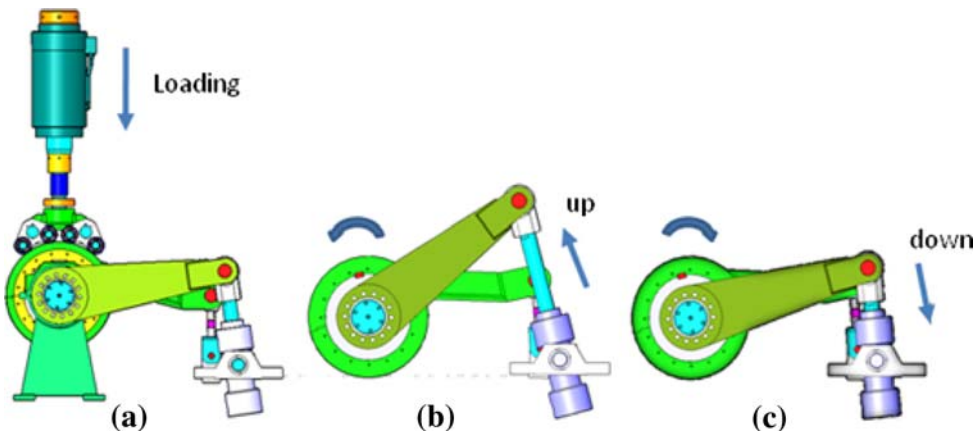

Fig. 2 Application of the test setup. **a** Loading, **b** counterclockwise rotation of the shaft, **c** clockwise rotation of the shaft

- This apparatus provides measurement of the normal and friction force among the bearing and the shaft, bearing's temperature during the application, and wear rate of the bearing's surface (by online measuring of the bushing displacement in two dimensions).
- The vertical load is applied through a transmission trolley, which provides uniform pressure distribution, while it allows small rotation of the bushing.

3 Kinematics of the Test Setup

Friction force plays a very important role in tribological analyses. Therefore, evaluation of the COF of materials in tribosystems is a key factor. In this study, the COF between the composite bearing and the steel shaft is calculated by using the measured factors.

Figure 3 depicts a schematic view of the loading and kinematics of the test rig. The parameters of the figure are

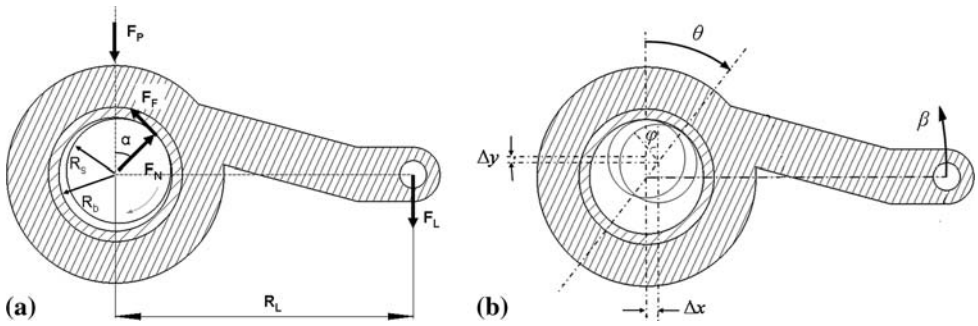

Fig. 3 Schematics of the acting forces and kinematics of the setup. **a** Acting forces, **b** kinematics

F_P loading actuator force; F_L force on the lever arm; F_F friction force between composite bearing and shaft; F_N normal force on composite bearing; R_S shaft radius; R_b bearing radius; R_L distance between the action points of F_P and F_L; and α rolling angle.

During the test F_P is assumed to be constant. And although due to a very small deviation of the hydraulic piston from its position, it is supposed to be vertical. Since the displacement of the bushing remains small, the force in the load cell F_L can also be considered vertical. According to Coulomb law [12], the COF is the ratio of the tangential and normal reaction force components:

$$\mu = \frac{F_F}{F_N} \tag{1}$$

F_F and F_N are derived from the following equilibrium equations:

$$F_F = \frac{R_L}{R_b} \cdot F_L \tag{2}$$

$$F_N = \left[(F_P + F_L)^2 - \left(F_L . \frac{R_L}{R_b} \right)^2 \right]^{1/2} \tag{3}$$

$$\sin\alpha = \frac{R_L}{R_b} \cdot \left(\frac{F_L}{F_P + F_L} \right) \tag{4}$$

Substituting the obtained equations for F_F and F_N from Eqs. 2 and 3 in Eq. 1, the COF becomes

$$\mu = \tan\ \alpha = \frac{1}{\left[\left(\frac{R_b}{R_L} \right)^2 \cdot \left(\frac{F_P + F_L}{F_L} \right)^2 \right]^{1/2}} \tag{5}$$

In the journal bearing application when the shaft starts to rotate, the bearing will initially roll up to a certain angle of inclination and will then start to slip [13, 14]. Therefore, if the shaft rotates continuously the process reaches to the steady-state sliding conditions after the first rolling step. The tangent of the inclination angle is the COF. If the elastic deformation of the load cell and the clearances of its both sides' connections are ignored, the kinematics of the shaft rolling in the bearing can be expressed as:

$$\left(\frac{d\beta}{dt} - \frac{d\theta}{dt} \right) \Big/ \left(\frac{d\varphi}{dt} - \frac{d\theta}{dt} \right) = \frac{R_s}{R_b} \tag{6}$$

In this equation, $d\beta/dt$, $d\theta/dt$, and $d\varphi/dt$ describe, respectively, rotating velocity of the bushing, rotating velocity of the shaft center, and rotating velocity of the shaft around its center. Since the lever arm prevents the rotation of the bushing, $d\beta/dt = 0$ and Eq. 6 will be simplified to

$$-\frac{d\theta}{dt} \Big/ \left(\frac{d\varphi}{dt} - \frac{d\theta}{dt} \right) = \frac{R_s}{R_b} \tag{7}$$

Solving the equation will result into

$$\varphi = \theta \cdot \frac{R_s - R_b}{R_s} \tag{8}$$

Once the angle θ reaches to α, this relation is no longer valid because the shaft starts to slide instead of rolling. In practice, the static COF differs from the dynamic COF. Therefore, there are two rolling angles α_S and α_D, which correspond to the static and dynamic COF. When the shaft starts to rotate it rolls up to $\theta = \alpha_S$, and then it drops to $\theta = \alpha_D$ and sliding occurs in the contact [14].

4 Finite-Element Modeling

Although the experimental method provides a good estimate of the forces on the bearing, it does not give detailed information about the contact stress distribution. Therefore, in order to study the stress distribution, numerical simulations are employed. In this article, the kinematics of the test rig is modeled by FEM method.

The traditional method of analyzing these kinds of rolling and sliding contacts is the Lagrangian formulation. In the Lagrangian approach, the nodal points are attached to the material points, thus the motion of the material during the process is followed. Hence, it is easy to follow the history of material deformation.

Figure 4 depicts a simple model of the meshing of the journal bearing application with the Lagrangian method.

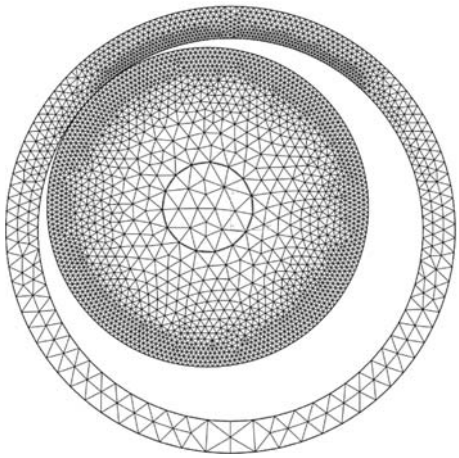

Fig. 4 Meshing of the journal bearing application with Lagrangian method

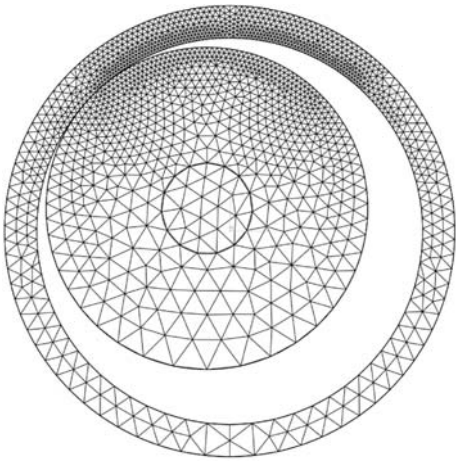

Fig. 5 Meshing of the journal bearing application with mixed Lagrange–Euler method

Both the shaft and the bearing have a cylindrical profile, and the inside surface of the bearing is in contact with the outside surface of the shaft. At first, both surfaces must be discretized with small elements to get a feasible approximation of cylindrical geometry. Moreover, in the contact area much finer meshes are necessary to find out a smooth contact line.

Since the bearing motion is small, a rough calculation contact area can be predicted and a finer mesh is localized just inside the contact region. The meshing is more critical for the shaft since it rotates and the contact points change in time. Therefore, the mesh-refined area is larger than that of the bearing, and in fully rotary motion the whole outer surface of the shaft must be meshed very finely.

To summarize, Lagrangian analysis is computationally expensive since a transient analysis must be performed and very fine meshing is required on the shaft surface.

Another possibility to simulate this problem is Eulerian method, in which attention is focused on the motion of the material through a stationary control volume. The advantage in this method is that Eulerian elements do not deform with the material. Therefore, regardless of the magnitude of the deformation in process, Eulerian elements retain their original shape.

The limitation of the Eulerian method is simulation of the free boundaries. In this approach, it is harder to follow the material deformation history since the mesh is fixed in space and is not distorted. However, the boundary of the deformation region should be known a priori, because it cannot be easily updated during the deformation. Indeed, if in an Eulerian simulation the boundaries of the model change, new control volumes have to be created, which is difficult to deal with [15].

An alternative approach which combines the advantages of both Lagrangian and Eulerian formulations is the mixed Lagrangian–Eulerian method. In this approach, the mesh can have a motion independent of material deformation. Consequently, the motion of the mesh can be designed in accordance with the nature of deformation, and thus mesh distortion is avoided on one hand and the boundaries are updated on the other hand [16].

Therefore, the advantage of the mixed Lagrangian–Eulerian method is localization of the mesh deformations to a certain restricted area of the shaft in contact with the bearing. The finite-element mesh describing the shaft does not undergo the large rigid body rotating motion. This means that a fine mesh is only required close to the contact zone. Figure 5 schematically shows the meshing of the journal bearing application in this method.

In this article, kinematics of the test setup is simulated as a quasi-static model via the mixed Lagrangian–Eulerian method, by ABAQUS finite-element code [17].

5 Friction

Experimental data show that the friction coefficient opposing the initiation of slipping from a sticking condition is different from the friction coefficient which opposes established slipping. The former is typically referred to as the "static" friction coefficient, and the latter is referred to as the "dynamic" friction coefficient. Typically, the static friction coefficient is higher than the dynamic friction coefficient.

The static friction coefficient corresponds to the value measured at zero slip rate, and the dynamic friction coefficient corresponds to the value measured at non-zero slip rate. In reality, the value of static friction typically increases if the two surfaces stay longer in stationary contact [18]. In general, the increase in the static friction to

an asymptote is so quick that we suppose that the static friction has a constant value.

In these tests, the stationary time in each cycle is not so long that an obvious change in static friction could be observed. It is assumed that the friction coefficient decays exponentially from the static value to the dynamic value according to the formula

$$\mu = \mu_D + (\mu_S - \mu_D) \cdot e^{-d_c \dot{\gamma}_{eq}} \tag{9}$$

where μ_D is the dynamic friction coefficient, μ_S is the static friction coefficient, d_c is a user-defined decay coefficient, and $\dot{\gamma}_{eq}$ is the slip rate [19].

Based on the experimental data, the parameters of the equation are defined and then the friction coefficient will be calculated correlated to the slip rate.

6 Material Modeling

The test bearing is a composite of a phenolic resin, polyester reinforcing fibers, and PTFE filling for internal lubrication. This bearing is an orthotropic material with the engineering constants shown in Table 1.

Once the engineering constants of the material are known, the stiffness coefficients C_{ij} and compliance coefficients S_{ij} are calculated. For an orthotropic material subjected to a three-dimensional state of stresses, the compliance matrix **S** equals (in this model, indexes 1, 2, and 3, respectively, indicate the radial, tangential, and axial coordinates).

$$\mathbf{S} = \begin{pmatrix} S_{11} & S_{12} & S_{13} & 0 & 0 & 0 \\ S_{21} & S_{22} & S_{23} & 0 & 0 & 0 \\ S_{31} & S_{32} & S_{33} & 0 & 0 & 0 \\ 0 & 0 & 0 & S_{44} & 0 & 0 \\ 0 & 0 & 0 & 0 & S_{55} & 0 \\ 0 & 0 & 0 & 0 & 0 & S_{66} \end{pmatrix} \tag{10}$$

And the compliance coefficients are

Table 1 Engineering constants of the composite bearing

E_{rr} (GPa)	2.75
E_{tt} (GPa)	10.00
E_{zz} (GPa)	10.00
G_{rt} (GPa)	1.00
G_{tz} (GPa)	4.00
G_{rz} (GPa)	1.00
υ_{rt}	0.165
υ_{tz}	0.250
υ_{rz}	0.068

r radial coordinate, t tangential coordinate, z axial coordinate

$$\begin{aligned} S_{11} &= \frac{1}{E_{rr}}; \quad S_{12} = -\frac{\upsilon_{tr}}{E_{tt}}; \quad S_{13} = -\frac{\upsilon_{zr}}{E_{zz}} \\ S_{21} &= -\frac{\upsilon_{rt}}{E_{rr}}; \quad S_{22} = \frac{1}{E_{tt}}; \quad S_{23} = -\frac{\upsilon_{zt}}{E_{zz}} \\ S_{31} &= -\frac{\upsilon_{13}}{E_{rr}}; \quad S_{32} = -\frac{\upsilon_{tz}}{E_{tt}}; \quad S_{33} = \frac{1}{E_{zz}} \\ S_{44} &= \frac{1}{G_{tz}}; \quad S_{55} = \frac{1}{G_{rz}}; \quad S_{66} = \frac{1}{G_{rt}} \end{aligned} \tag{11}$$

And

$$E_{rr}\upsilon_{tr} = E_{tt}\upsilon_{rt}; \quad E_{rr}\upsilon_{zr} = E_{zz}\upsilon_{rz}; \quad E_{zz}\upsilon_{tz} = E_{tt}\upsilon_{zt} \tag{12}$$

The stiffness matrix **C** is the inverse of the compliance matrix. Therefore, by measuring the engineering constants, the stiffness matrix of the material is extracted and applied in the finite-element equations [20].

7 Boundary Conditions for Two-Dimensional Plane Strain Analysis

Looking again at the structure of the test rig provides that the geometry of the bearing and bushing consists of uniformly extruded sections along the shaft's axis. In addition, the hydraulic piston applies a uniformly spread pressure on the bushing over the same axis. Therefore, considering the width of the bearing (120 mm), which is long enough to prevent the strain in the axial direction, a two-dimensional plane strain model can provide careful investigation of the stress distribution on the bearing as well as the kinematic modeling of the machine.

Figure 6 depicts the boundary conditions and meshing of the two-dimensional plane strain model for the test rig. This model includes 16,939 high-accuracy quadratic elements. The bearing and the contact surfaces are discretized with quadrilateral elements and the other regions with triangular.

In this research, study of the stress distribution in the loading-subassembly is not an objective. Therefore, the loading-subassembly is simplified by a mechanism composed of four springs and two rigid rollers.

To provide accurate radial pressure on the bushing, the rotational degree of freedom of the rollers' reference points are independent of the springs' nodes. Finally, because the COF in the roller bearings of the transmission trolley is very low, the friction between the rollers and the bushing is equated to zero.

The friction torque load-cell is simulated as a combination of a solid beam and two rigid pins. The kinematics of the rigid pins is coupled to the ends of the load-cell.

Hinge-A and hinge-B are, respectively, the connection between load-cell and bushing, and load-cell and support. In order to validate the analytical calculations, at the first step of simulations, these contact boundaries are simulated without friction.

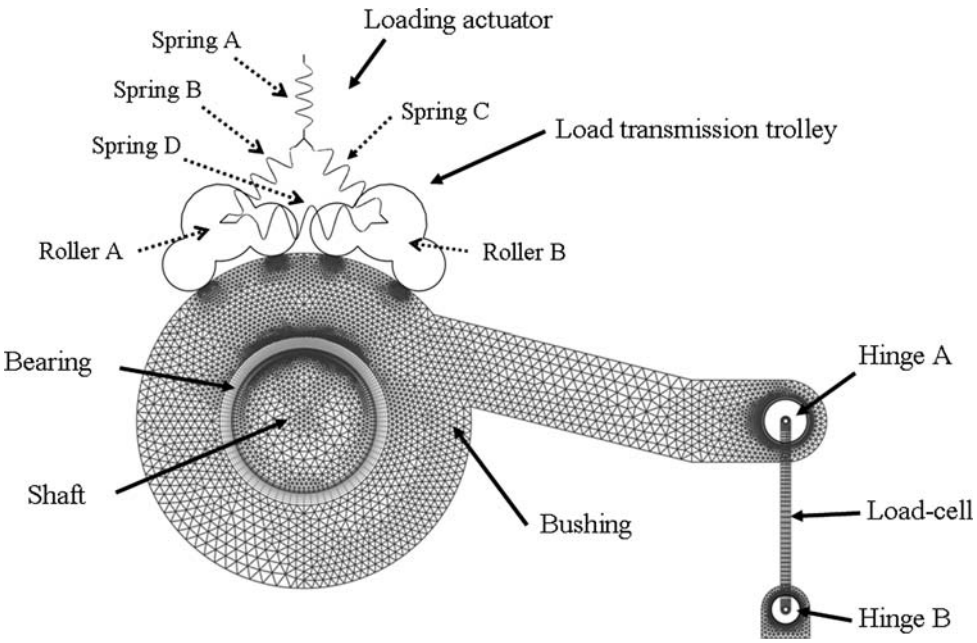

Fig. 6 Two-dimensional finite-element model

Finally, the rotational oscillation of the shaft is provided by Eulerian formulation, and its deformation under the contact force with the bearing is simulated by Lagrangian contact formulation.

8 Experimental Results

The tests were performed on a composite bearing under the conditions shown in Table 2.

Figure 7 shows the experimental results for the COF between the composite bearing and the shaft.

After applying the vertical load by the loading actuator, the shaft starts to rotate. At the start, the driving load should overcome the static friction, and as soon as slip occurs, the friction value decreases to the dynamic friction. When the motion direction of the drive piston changes, the shaft rotation is reversed, thus there is a point in each cycle that the velocity of the shaft is zero. Hence at the start of each cycle, the friction value rises to static friction and then decreases to dynamic friction. These results show that the static friction coefficient between the bearing and the shaft is 0.145, and the dynamic COF is 0.115.

Table 2 Test conditions

Bearing diameter (mm)	300
Bearing thickness (mm)	25
Normal load by hydraulic actuator (kN)	100
Amplitude of drive piston (mm)	5
Frequency of drive piston (Hz)	0.5
Clearance between the shaft and bearing (mm)	1.1
Clearance between the load cell pins and correlated bushings (mm)	0.1

Figure 8 depicts the friction force (F_F) and normal force (F_N), obtained from the experimental measurements. As argued in the previous paragraphs, due to the static COF at the start of each cycle, the friction force graph shows a spike, and when sliding occurs it decreases. It is obvious that when the direction of the rotation changes, the direction of the friction force also will change.

This fluctuation in the friction force generates a relative variation in the normal force between bearing and shaft. Once the direction of the friction force changes, the normal force reduces. The maximum and minimum values of the normal force between the shaft and the bearing are 102 and 96.3 kN, respectively.

In Fig. 9, the measured horizontal displacement of the bushing is shown. At the moment that the shaft motion tends to overcome the static friction force, the bearing sticks to the shaft. In this moment regarding the direction of the rotation, the bushing system moves forward or backward. Once the contact condition changes from rolling to sliding, the bearing slides back and the shaft slides against the bearing in a fixed position. The horizontal displacement of the bushing varies between $+0.1$ and -0.1 mm.

Figure 9 also shows that at each cycle of the test the rolling angle is about 8°, and the sliding angle is 6.5°.

9 Simulation Results

From the experimental data, the parameters of Eq. 9 are defined. For the selected bearing, the static COF is 0.145,

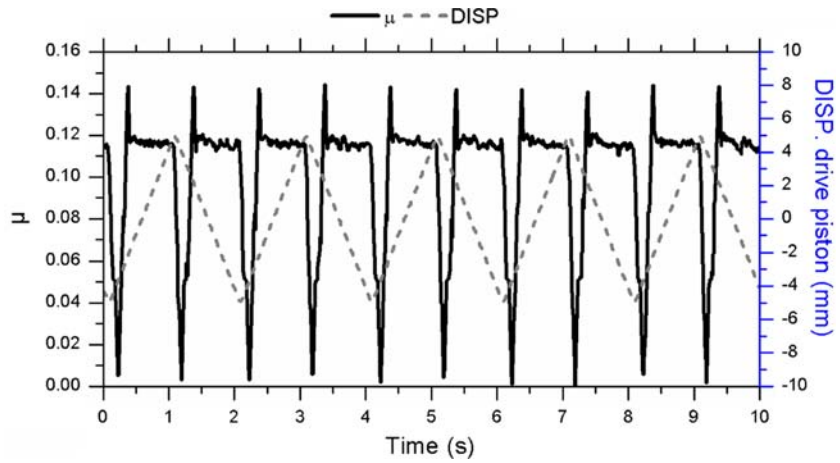

Fig. 7 Measured values of the drive piston's displacement and calculated values of the COF between the composite bearing and the shaft

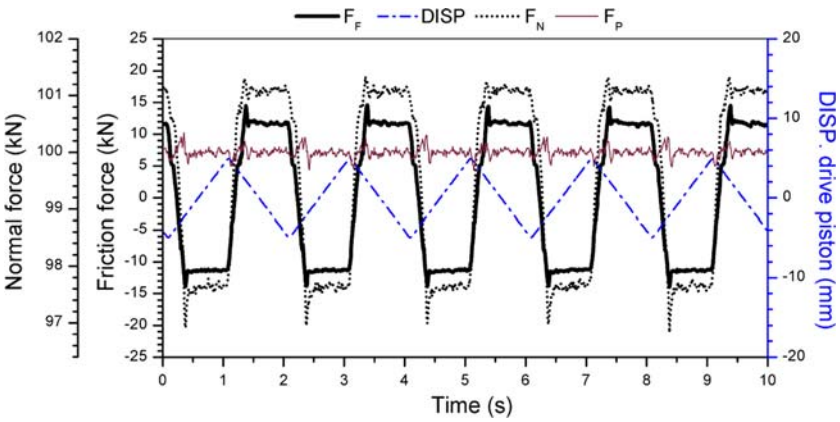

Fig. 8 Experimental measurements of the friction and normal forces between the composite bearing and the shaft. F_F friction force, F_N normal force, F_P applied load by loading piston, *DISP* displacement of driving piston

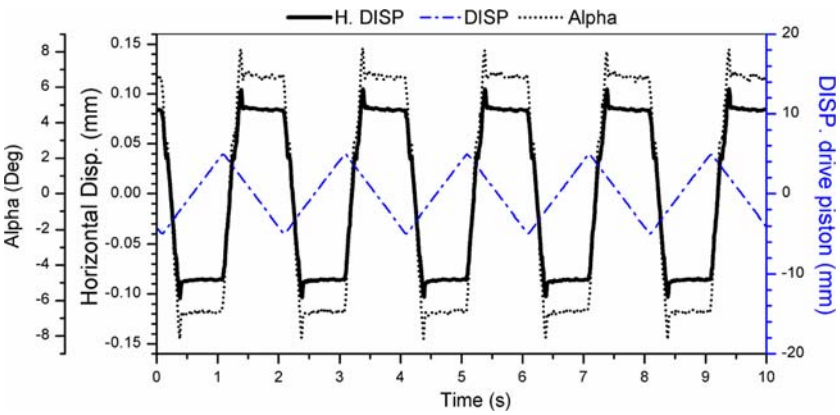

Fig. 9 Measured values of the horizontal displacement of the bushing, and rolling and sliding angles calculated form the experimental data. *H.DISP* horizontal displacement of bushing, *Alpha* angle, *DISP* displacement of driving piston

the dynamic COF for the infinite slip rate is 0.115, and the user-defined coefficient based on the experimental information is 1000 (s m^{-1}). Therefore, the friction model in the finite-element calculations is

$$\mu = 0.115 + (0.145 - 0.115) \cdot e^{-1000\dot{\gamma}_{eq}} \quad (13)$$

Figure 10 shows the variation of the friction coefficient versus the slip rate between the shaft and the bearing.

Figure 11 shows the main steps of the radial stress distribution on the composite bearing. In the first step, after applying 100 kN force, radial stress in the bearing is built up. The stresses are symmetrically distributed along the loading axis, and the maximum radial stress in the center of the contact line equals 8.5 MPa. After the loading is completed, the shaft starts to rotate in the clockwise direction. By rotating the shaft, stress contours start to

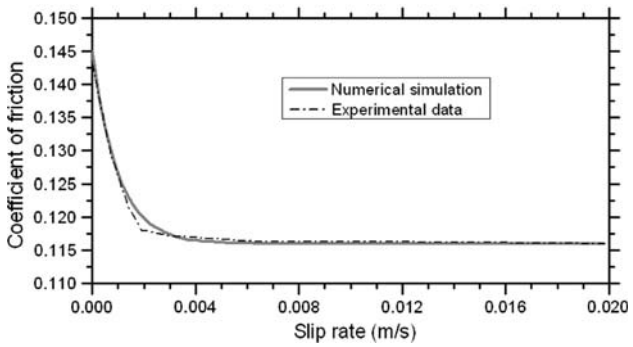

Fig. 10 Exponential decay friction model for FEM simulation

move to the left and at the sliding point remain fixed (see step 2), and when the shaft rotates in the counterclockwise direction, stress contours move to the right (step 3).

Figure 12 shows the frictional shear stress and contact pressure distribution on the bearing surface. At the beginning of each cycle in the rolling contact condition, the stress contours slightly incline more to the left and right, respectively, in the clockwise and counterclockwise shaft rotations, and also the values of the stresses slightly change. This fluctuation in the contact stresses, both in contact pressure and frictional shear stresses, is due to the effect of the static COF.

As can be seen, after applying the vertical load in the model, due to the elastic deformation of the bearing, there is a very low amount of shear stresses on the contact surface which is symmetrically distributed over the loading axes. Then, by oscillation of the shaft at each cycle, the maximum value of the shear stress at the beginning of the cycle is about 0.2 MPa higher than in the sliding condition. The maximum value of the shear stress is about 1.25 MPa at the beginning of each cycle during the rolling contact.

Tangential stress distribution is shown in Fig. 13. In the loading step, highest compressive stresses are initiated at the center of the contact zone and above the contact center in the vicinity of the bushing. The uppermost tensile stresses are appeared in the corners of the contact area.

When the shaft rotates in the clockwise direction, the compressive stresses of the surface layer are inclined to the right, and tensile stresses are inclined to the end of the contact zone at the left. With the counter clockwise rotation of the shaft, the compressive and tensile stresses on the bearing's surface, respectively, move to the left and right. In both conditions, another high compressive stress

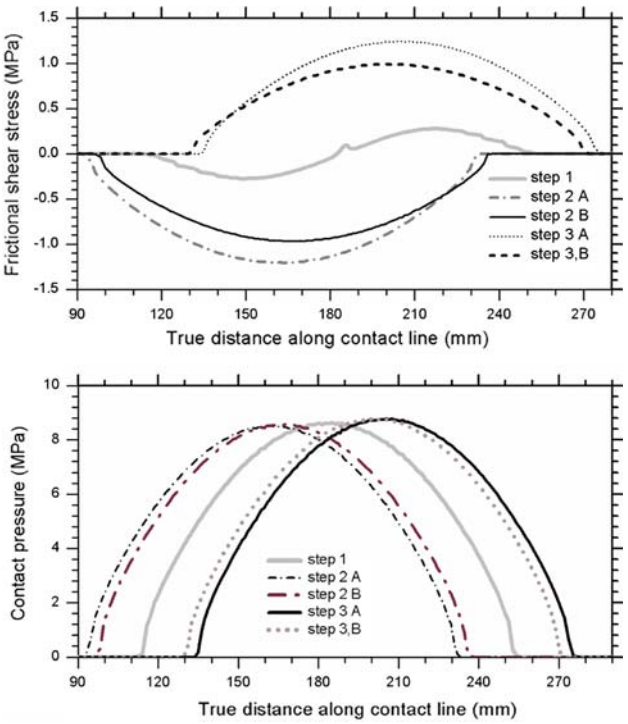

Fig. 12 Distribution of the frictional shear stresses and contact pressure on the contact surface of the composite bearing. *Step 1* loading without motion of the shaft, *step 2A* beginning of the first cycle, *step 2B* sliding point of the first cycle, *step 3A* beginning of the second cycle, *step 3B* sliding point of the second cycle

Fig. 11 Radial stress distribution on the composite bearing

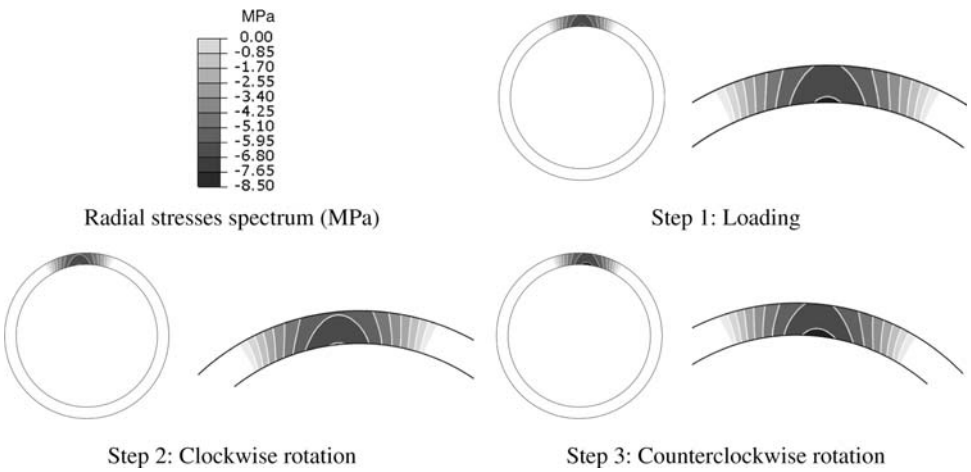

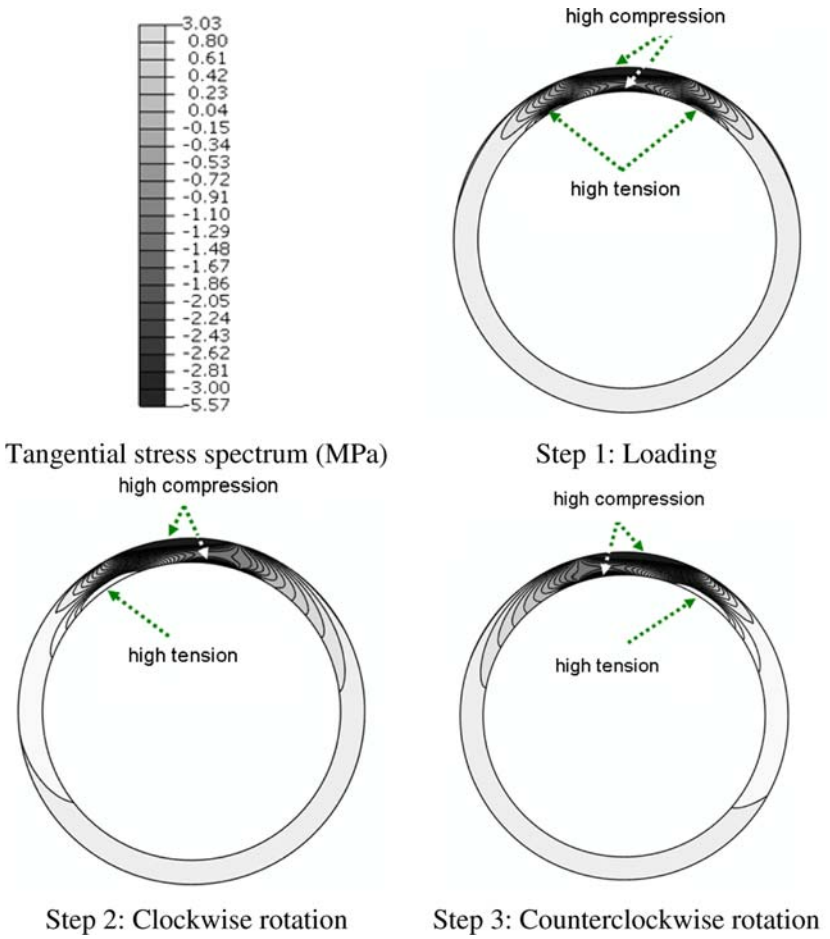

Fig. 13 Tangential stress distribution on the composite bearing

gradient is appeared above the contact center in the vicinity of the bushing.

Since the tangential compressive strength of the bearing is its' weakest strength parameter, these stresses can be important in the failure analysis of the bearing.

In this test, a simple analysis based on the maximum stress theory provides that there is no failure in the bearing [20]. The strength components of the bearing are as below [21].

Compressive radial strength = 305 MPa
Compressive tangential strength = 28 MPa
Tensile tangential strength = 80 MPa
Shear strength = 80 MPa

Based on the represented simulation results, the maximum compressive radial stress, compressive tangential stress, tensile tangential stress, and shear stress in the bearing are 8.5, 5.57, 3.03, and 1.3 MPa, respectively. All these values are far below the ultimate strength of the bearing.

Figure 14 shows the FEM simulation results for the friction and normal forces between the shaft and bearing. Because the first cycle starts from the mean of the oscillation amplitude, the time interval of the first period is half of the others. For easiness, the states of the clockwise and counterclockwise rotations are labeled with cycle-A and cycle-B.

In cycle-A, the static and dynamic friction forces are 13.80 and 11.10 kN, respectively. Likewise, in cycle-B these values are 14.30 and 11.40 kN. The relevant experimental data for the static and dynamic friction forces are 13.80 and 11.30 kN, respectively, in cycle-A, and 14.30 and 11.60 kN, respectively, in cycle-B (Fig. 8). Consequently, the simulation and experimental results are in a very good agreement for the static friction force, and there is a very small deviation, 0.20 kN, in the dynamic friction force. This minor error comes from different sources. On one hand, parameters like vibration of the system and very small instabilities in hydraulic actuators can generate some noise. On the other hand, a very small divergence between the implemented exponential function and the measured friction coefficient can be a source of error in the numerical calculations. However, in a test with this scale due to many parameters like microscopic nonuniformities and environmental conditions, it is almost impossible to achieve the results that can be fitted perfectly to an exponential

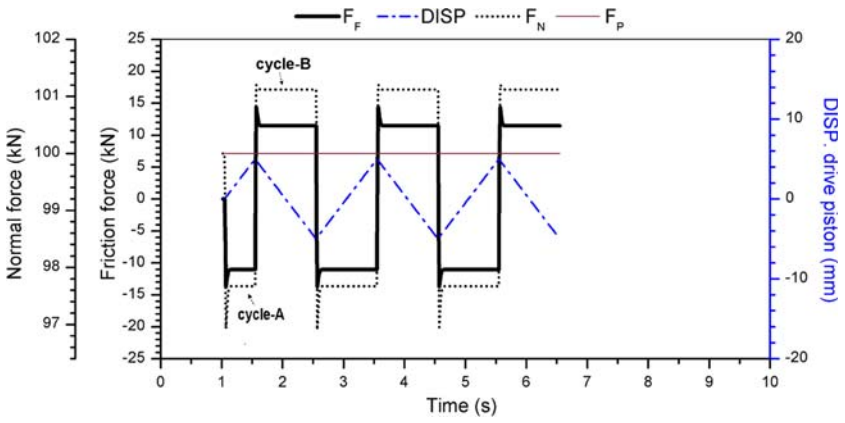

Fig. 14 FEM results of the friction and normal forces between the composite bearing and shaft. F_F friction force, F_N normal force, F_P applied load by loading piston, *DISP* displacement of driving piston

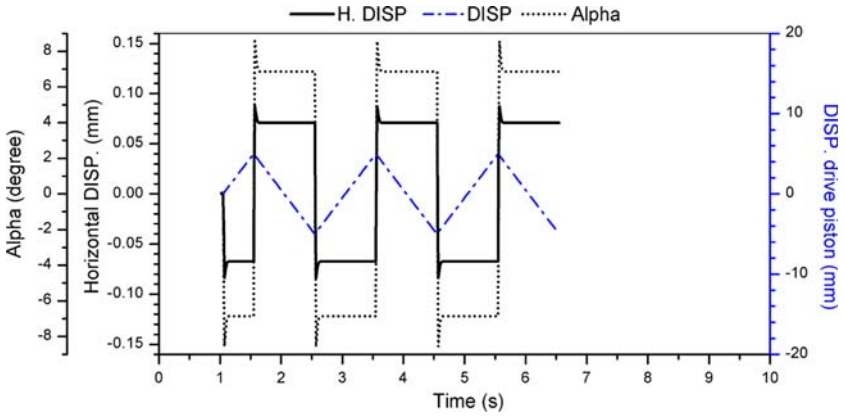

Fig. 15 FEM results of horizontal displacement of the bushing and rolling and sliding angles of the bearing, *H.DISP* horizontal displacement of bushing, *Alpha* angle, *DISP* displacement of driving piston

equation. At all, these minor errors are almost unavoidable and considering the scale of the test is acceptable.

In cycle-A, the normal force rises from 96.90 kN in the rolling state to 97.70 kN in the sliding state, whereas in cycle-B it decreases from 101.20 to 101.10 kN. These values also correspond closely to the experimental data shown in Fig. 8. The experimental outputs show that in cycle-A the normal force increases from 96.90 to almost 97.70 kN, whereas in cycle-B decreases from 101.25 to 101.10 kN.

Figure 15 shows the rolling angle of the bearing and horizontal displacement of the bushing. At the start of each cycle, the bearing rolls up about 8° due to the static COF, and then slides back about 1.5° to the sliding position. These values also correspond closely to the calculated rolling and sliding angles from the experimental data (see Fig. 9).

In cycle-A, the horizontal displacement is 0.086 mm in the rolling and 0.069 mm in the sliding states, and in cycle-B it is 0.088 mm in the rolling and 0.071 mm in the sliding states. Comparing these results with the experimental data, shown in Fig. 9, gives about 15% difference.

In the setup, there are two big self-aligning roller bearings used in the shaft supports. The internal clearance of these roller bearings can provide a very small displacement in the shaft, which is not accounted for in the simulation. This small deviation can be the influence of the internal clearance of these shaft supports. Hence, experimental records for horizontal displacement of the bushing are a little bigger than numerical calculations.

10 Conclusion

A new servo-controlled test setup was introduced to study the tribological behavior of the large-scale composite bearings under the reciprocating angular movements. A test was performed on a polyester-based composite bearing, and the friction force, normal force, and kinematics of the bearing were studied.

Besides these empirical investigations, a mixed Lagrangian–Eulerian finite-element method was used to evaluate the distribution of the stresses and strains on the bearing. The bearing was simulated as an orthotropic material, and the static and dynamic friction conditions were applied through an exponential function.

The simulation results are in a very good agreement with the experimental outputs, and show that the combination of the Lagrange and Euler formulations is a very convenient

tool to simulate journal bearing applications. With this method not only the calculation time is reduced, but also the contact simulating precision is enhanced.

Considering the cost of the experimental methods in large-scale testing, these simulations are very helpful tools to analyze and predict the effect of the mechanical design parameters and material properties of the composite journal bearings.

References

1. Johnson, K.L.: Contact Mechanics. Cambridge University Press, Cambridge, MA (1985)
2. Kim, M.R., Taylor, J.O., Batten, B.L.: The evolution of filament wound bearings. Sampe. J. **39**, 10–15 (2003)
3. Kawakame, M., Bressan, J.D.: Study of wear in self-lubricating composites for application in seals of electric motors. In: 3rd Brazilian Congress of Manufacturing Engineering, pp. 74–80. Elsevier Science Sa, Joinville, Brazil (2005)
4. Liu, Y., Schaefer, J.A.: The sliding friction of thermoplastic polymer composites tested at low speeds. Wear **261**, 568–577 (2006)
5. Elsayed, A.A., Elsherbiny, M.G., Aboelezz, A.S., Aggag, G.A.: Friction and wear properties of polymeric composite-materials for bearing applications. Wear **184**, 45–53 (1995)
6. Friedrich, K., Flöck, J., Váradi, K., Néder, Z.: Experimental and numerical evaluation of the mechanical properties of compacted wear debris layers formed between composite and steel surfaces in sliding contact. Wear **251**, 1202–1212 (2001)
7. Friedrich, K., Goda, T., Varadi, K., Wetzel, B.: Finite element simulation of the fiber-matrix debonding in polymer composites produced by a sliding indentor: Part I. Normally oriented fibers. J. Compos. Mater. **38**, 1583–1606 (2004)
8. Goda, T., Varadi, K., Wetzel, B., Friedrich, K.: Finite element simulation of the fiber-matrix debonding in polymer composites produced by a sliding indentor: Part II. Parallel and anti-parallel fiber orientation. J. Compos. Mater. **38**, 1607–1618 (2004)
9. Lee, D.G., Kim, S.S.: Design of the hybrid composite journal bearing assembled by interference fit. Compos. Struct. **75**, 222–230 (2006)
10. Lee, D.G., Kim, S.S.: Failure analysis of asbestos-phenolic composite journal bearing. Compos. Struct. **65**, 37–46 (2004)
11. Biyiklioglu, A., Cuvalci, H., Adatepe, H., Bas, H., Duman, M.S.: A new test apparatus and method for friction force measurement in journal bearings under dynamic loading. Exp. Tech. **29**(5), 22–24 (2005)
12. Persson, B.N.J.: Sliding Friction: Physical Principles and Applications, p. 13. Springer, Berlin (1998)
13. van Beek, Av: Machine Lifetime Performance and Reliability. Delft University of Technology, (2004)
14. Van Wittenberghe, J., Ost, W., Rezaei, A., De Baets, P., Zsidai, L., Kalacska, G.: Test setup for friction force measurements of large-scale composite bearings. Exp. Tech. **33**, 45–50 (2009)
15. Bathe, K.-J.: Finite Element Procedures. Prentice Hall, Englewood, NJ (1996)
16. Belytschko, T., Liu, W.K., Moran, B.: Nonlinear Finite Elements for Continua and Structures, pp. 393–443. Wiley, New York (2000)
17. ABAQUS V6.8 Analysis User's Manual: Analysis Procedures
18. Mate, C.M.: Tribology on the Small Scale. Oxford University Press, Oxford (2008)
19. Oden, J.T., Martins, J.A.C.: Models and computational methods for dynamic friction phenomena. Comput. Methods Appl. Mech. Eng. **52**, 528–634 (1985)
20. Herakovich, C.T.: Mechanics of Fibrous Composites. John Wiley & Sons, New York (1998)
21. Kuhne Multiglide T814 Datasheet, kuhne, http://www.kuhne.nl/